

Situational Graphs for Robot Navigation in Structured Indoor Environments

Hriday Bavle¹, Jose Luis Sanchez-Lopez¹, Muhammad Shaheer¹,
Javier Civera² and Holger Voos¹

Abstract—Autonomous mobile robots should be aware of their *situation*, understood as a comprehensive understanding of the environment along with the estimation of its own state, to successfully make decisions and execute tasks in natural environments. 3D scene graphs are an emerging field of research with great potential to represent these *situations* in a joint model comprising geometric, semantic and relational/topological dimensions. Although 3D scene graphs have already been utilized for this, further research is still required to effectively deploy them on-board mobile robots.

To this end, we present in this paper a real-time online built Situational Graphs (*S-Graphs*), composed of a single graph representing the environment, while simultaneously improving the robot pose estimation. Our method utilizes odometry readings and planar surfaces extracted from 3D LiDAR scans, to construct and optimize in real-time a three layered *S-Graph* that includes a robot tracking layer where the robot poses are registered, a metric-semantic layer with features such as planar walls and our novel topological layer constraining higher-level features such as corridors and rooms. Our proposal does not only demonstrate state-of-the-art results for pose estimation of the robot, but also contributes with a metric-semantic-topological model of the environment.

I. INTRODUCTION

Mobile robots require rich semantic descriptions of the key elements of a scene to understand the situation around them, to estimate accurate task-oriented maps of their surrounding environment and to localize themselves into them. Geometric LiDAR SLAM methods such as [1], [2] and [3] are essential for safe navigation but they are unable to identify these key elements, which compromises among others high-level task definitions and the localization and mapping performance in cluttered, repetitive or dynamic environments. Semantic SLAM methods like [4], [5] and [6] utilize key semantic elements from the environment but

*This work was partially funded by the Fonds National de la Recherche of Luxembourg (FNR), under the projects C19/IS/13713801/5G-Sky, by a partnership between the Interdisciplinary Center for Security Reliability and Trust (SnT) of the University of Luxembourg and Stugalux Construction S.A., by the Spanish Government under Grant PGC2018-096367-B-I00 and by the Aragón Government under Grant DGA T45 17R/FSE. For the purpose of Open Access, the author has applied a CC BY public copyright license to any Author Accepted Manuscript version arising from this submission

¹Authors are with the Automation and Robotics Research Group, Interdisciplinary Centre for Security, Reliability and Trust, University of Luxembourg. Holger Voos is also associated with the Faculty of Science, Technology and Medicine, University of Luxembourg, Luxembourg. {hriday.bavle, joseluis.sanchezlopez, muhammad.shaheer, holger.voos}@uni.lu

²Author is with I3A, Universidad de Zaragoza, Spain jcivera@unizar.es

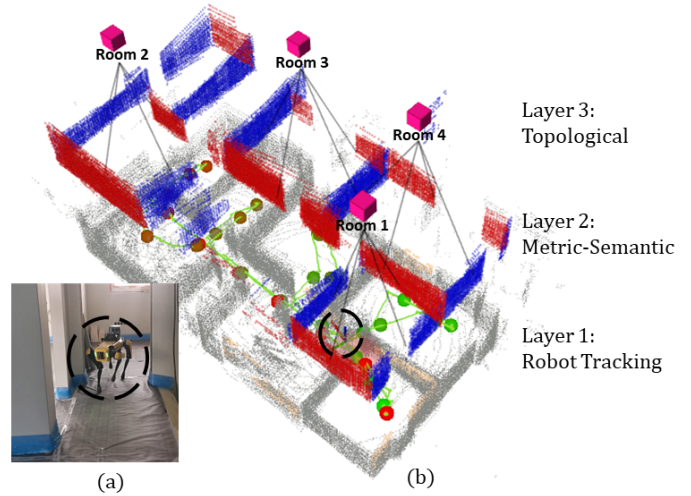


Fig. 1: *S-Graph* generated using the legged robot in (a) corresponding to a real construction site. The graph in (b) can be divided into three sub-layers: 1) The robot tracking layer estimates the sensor poses and creates a map of keyframes. 2) The metric-semantic layer creates a plane-based map connected with the keyframes. 3) The topological layer links the planes and the room/corridor representations using novel factors proposed on this work.

do neither consider nor model the relation between these elements to further constraint their geometry, which would improve their performance and the understanding of the situation around the robot.

Recent approaches such as [7], [8] model the scene as a graph, in order to efficiently represent the environment and its semantic elements in a hierarchical representation with structural and topological constraints between the elements. Scene graphs might enable the robots to understand and navigate the environment similarly to humans, using high-level abstractions (such as chairs, tables, walls) and the inter-connections between them (such as a set of walls forming a room or a corridor). Although works using scene graphs show promising results, there still exists a gap to connect such scene graphs with geometric SLAM methods that simultaneously optimize the robot poses along with the scene graph.

In this direction we present Situational Graphs (*S-Graphs*), which bridges geometric LiDAR SLAM and scene graphs. Our *S-Graphs* (Fig. 1) are divided into three layers, namely *Robot Tracking Layer*, *Metric-Semantic Layer* and *Topologi-*

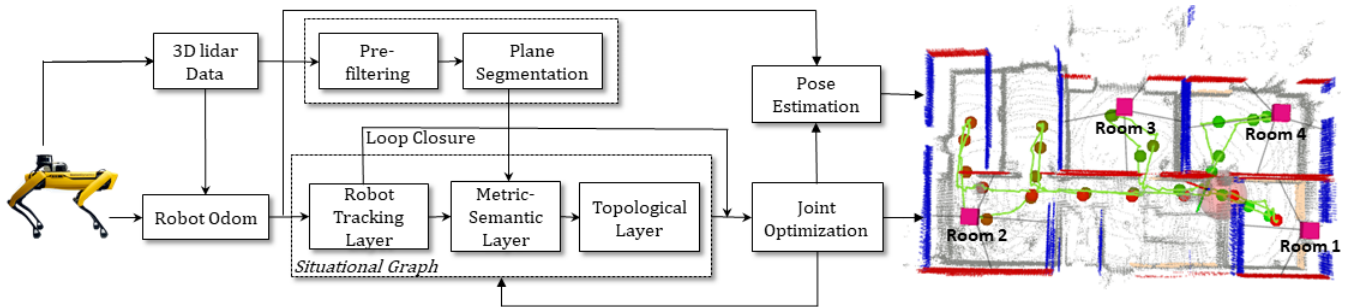


Fig. 2: Pipeline of the proposed *S-Graph* architecture, receiving 3D lidar measurements and robot odometry at a given time instant t , along with its filtering and planar extraction components. The figure also present the three layered situational graph along with the loop closure constraint, which are jointly optimized to update the robot pose and the *S-Graph*.

cal Layer. The robot tracking layer is the lowest level of the graph creating keyframes at regular time-distance intervals whose pose is constrained by odometry measurements. The metric-semantic layer extracts semantic elements at a given keyframe and maps them using their geometric constraints with respect to the keyframes. In our case we use pose-plane constraints from detected planar surfaces, thus optimizing mapped planes and robot keyframe poses. The topological layer is the highest level of the graph connecting the mapped planar surfaces to higher-level entities using suitable topological constraints, which in our case are the room and corridor factors. These factors add additional constraints over their corresponding plane features. In this manner, *S-Graphs* do not only optimize the robot poses but also the whole 3D scene graph jointly, comprising the mapped planar surfaces along with the corridor and room geometries.

As a summary, our main contributions in this paper are:

- A real-time implementation of *S-Graphs* using robot odometry and 3D LiDAR measurements with three hierarchical layers, optimizing the robot poses jointly with a high-level 3D representation the scene.
- The introduction of novel room and corridor factors into a graph formulation, that enable high-level representations of indoor scenes and constrain planar landmarks and robot poses.
- A thorough experimental evaluation on simulated and real scenarios, showing that in addition to representation advantages, our *S-Graph* model achieves state-of-the-art accuracy.

II. RELATED WORKS

A. Geometric SLAM

Geometric SLAM, using either visual sensors or 3D LiDAR, have been widely researched in the field of robotics in the last decades. We refer the reader to the survey in [9] for a broad perspective of the research in the field, and to ORB-SLAM2 [10] and LOAM [1] as two representative pipelines. Both of them estimate in real-time the global robot pose using visual/LiDAR measurements, as well as accurate 3D point clouds as map representation.

Focusing on LiDAR SLAM, similarly to LOAM and its variants [11], [12], methods like LIO-SAM [13], LIO-

MAPPING [14], HDL-SLAM [3] also estimate the robot poses and a 3D map, but with option of integrating additional sensor modalities such as IMU and GPS. Other methods such as like LIMO [15], LIRO [16] and LVI-SLAM [17] fuse visual and LiDAR measurements for simultaneous localization and mapping. Although these systems demonstrated significant progress in robustness and accuracy in the last years, they are limited for several application cases by their map representation. The lack of high-level semantically meaningful map representations reduces their robustness and hinders their use for interfacing with humans or defining object-based tasks.

B. Semantic SLAM

To improve the robustness and richness of representation of geometric SLAM, semantic SLAM has evolved with methods such as [4]. VPS-SLAM [5], [18] estimate a geometric map and add semantic objects in the environment for jointly optimizing the robot pose and semantic object landmarks. Methods like [19], [20] utilize object detections to create dense metric-semantic maps of the environment. Works using LiDAR sensors like LeGO-LOAM [21] incorporate ground planes and line edges as high-level features from segmented point cloud data to improve robot poses and map estimates when compared against LOAM. SA-LOAM [22] utilizes semantics from the environment like roads, buildings, traffic signs to improve the loop closure accuracy of LOAM. Similarly, methods like SUMA++ [6] utilize semantics to filter out dynamic objects improving the robot pose and the map quality. All the above methods provide improved environment representation as well as the map estimate, but lack the inclusion of structural/topological constraints between different semantic elements to further increase the robustness of the environmental understanding and reasoning for the robot. Similar to our approach, methods like π -LSAM [23], [24] utilize segmented planar features to create planar maps but as the other semantic SLAM approaches, they do not consider any topological/structural constraints between the planes.

C. Scene Graphs

Recent advances in computer vision have led to development of scene graphs, generating a comprehensive graph of

all the extracted semantic information from an environment along with the inter-relationships of the different semantic components within it. The pioneering work of 3D Scene Graph [7] creates an offline semi-autonomous framework using object detections over RGB images, generating a multi-layered hierarchical representation of the environment and its components, divided mainly in layers of camera, objects, rooms and building.

Rosinol et al. [25] extend the scene graph concept to environments with static and dynamic agents. It uses the Kimera Visual-Inertial Odometry (VIO) with object detection's to create a metric-semantic mesh which is then fed to scene generator creating the dynamic scene graph in an offline fashion. Though promising in terms of scene representation, a major drawback of these models is that they do not tightly couple the estimate of the scene graph with the state estimate of the SLAM framework, to simultaneously optimize them, thus generating a scene graph and a SLAM graph in an independent manner. The very recent work Hydra [26] presents research in the direction of real-time scene graph generation as well as its optimization using loop closure constraints. Our approach is aligned in a similar direction towards real-time scene graphs. However, compared to Hydra, ours creates the entire *S-Graph* as an optimizable factor graph, being constrained as a whole whenever planar landmarks are observed and specifically linking the planar landmarks with novel topological constraints.

Thus, in this paper, we present a framework to generating online and real-time *S-Graphs*, which bridges a gap in the current state-of-the-art: we incorporate the potential of scene graphs into traditional graph-SLAM frameworks by creating the multi-hierarchical models of the environment and simultaneously optimizing it along with the robot poses. We showcase state-of-the-art results in state estimation and 3D LiDAR mapping.

III. SITUATIONAL GRAPHS

A. Overview

An overview of the proposed approach is shown in Fig. 2. We define four reference frames: the map frame M , the odometry frame O , the robot frame R_t and the LiDAR frame L_t . The last two change with time as the robot moves but are rigidly related to each other. We separate the odometry and map frames to avoid that large state updates affect the navigation commands. We include in the state their relative transformation ${}^M\mathbf{x}_O$. Our pipeline receives as input the 3D LiDAR sensor measurements in frame L_t as well as odometry measurements from the robot sensors in frame R_t . Our global state \mathbf{s} is defined as

$$\mathbf{s} = [{}^M\mathbf{x}_{R_1}, \dots, {}^M\mathbf{x}_{R_T}, {}^M\boldsymbol{\pi}_1, \dots, {}^M\boldsymbol{\pi}_P, {}^M\boldsymbol{\rho}_1, \dots, {}^M\boldsymbol{\rho}_S, {}^M\boldsymbol{\kappa}_1, \dots, {}^M\boldsymbol{\kappa}_K, {}^M\mathbf{x}_O]^\top, \quad (1)$$

where ${}^M\mathbf{x}_{R_t}$, $t \in \{1, \dots, T\}$ are the robot poses at T selected keyframes, ${}^M\boldsymbol{\pi}_i$, $i \in \{1, \dots, P\}$ are the plane parameters of the P planes in the scene, ${}^M\boldsymbol{\rho}_j$, $j \in \{1, \dots, S\}$ contains the parameters of the S rooms and ${}^M\boldsymbol{\kappa}_k$, $k \in$

$\{1, \dots, K\}$ the parameters of the k corridors. We detail the specific form of these map elements later in Section III-D.

We will jointly optimize the state \mathbf{s} as follows

$$\hat{\mathbf{s}} = \arg \min_{\mathbf{s}} (c_{\mathbf{x}} + c_{\boldsymbol{\pi}} + c_{\boldsymbol{\rho}} + c_{\boldsymbol{\kappa}}) \quad (2)$$

where $c_{\mathbf{x}}$, $c_{\boldsymbol{\pi}}$, $c_{\boldsymbol{\rho}}$ and $c_{\boldsymbol{\kappa}}$ are cost functions related respectively with the robot tracking, metric-semantic and topological (room and corridor) layers respectively. We elaborate on them in Section III-D.

The overall pipeline can be divided into three main modules. The first one pre-filters the LiDAR measurements to remove noise and performs plane segmentation to detect and extract the planar surfaces. The second module computes the robot odometry either from LiDAR measurements or from the robot encoders. The third module is the LiDAR mapping, which generates the *S-Graph*. It first receives the robot odometry measurements to create a factor graph of robot keyframe poses as factor nodes at pre-defined distances. These nodes form the first layer of the *S-Graph*. It also receives the plane detections for the corresponding keyframes, which are classified either as vertical or horizontal planar nodes, forming in this manner the second layer of the *S-Graph*. Each of the mapped vertical planar nodes are further checked to assess if they belong a corridor or a room node. Four planar surfaces with some specific properties form a room node, and similarly planar surfaces in a specific configuration that we will detail later constitute a corridor node. The creation and model of appropriate corridor and room nodes and the edges modelling their relation to corresponding planar nodes comprise the third layer of the *S-Graph*.

B. Plane Extraction

Our plane extraction module receives the raw point cloud measurements from the 3D LiDAR sensor. We first down-sample the point cloud, and then remove gross outliers by filtering out points outside an interval defined by the average and standard deviation of the distances to the robot. This pre-processed point cloud is then passed to the plane segmentation module, that uses sequential RANSAC to detect all planar surfaces and gives a first estimation of their normals. In order to avoid the double-side issue mentioned in [24], we refer all normal orientations pointing to the LiDAR origin frame L_t by converting the plane normals as in [27].

$${}^{L_t}\boldsymbol{\Pi} = {}^{L_t}\mathbf{n}' \cdot {}^{L_t}d' \longrightarrow \begin{bmatrix} {}^{L_t}\mathbf{n} \\ {}^{L_t}d \end{bmatrix} = \begin{bmatrix} {}^{L_t}\boldsymbol{\Pi} / \|{}^{L_t}\boldsymbol{\Pi}\| \\ \|{}^{L_t}\boldsymbol{\Pi}\| \end{bmatrix} \quad (3)$$

where ${}^{L_t}\mathbf{n} = [{}^{L_t}n_x, {}^{L_t}n_y, {}^{L_t}n_z]^\top$ is the plane normal and ${}^{L_t}d$ is the distance to the origin, both in the LiDAR frame.

C. Robot Odometry

We use the Voxelized Generalized Iterative Closest Point (VGICP) in [28]. This voxelized version of GICP aggregates the voxel distribution on each point, parallelizing the optimization and achieving similar accuracy to GICP but substantially faster (it runs at 30 Hz on a low-end CPU). Alternatively, as we run our experiments on legged

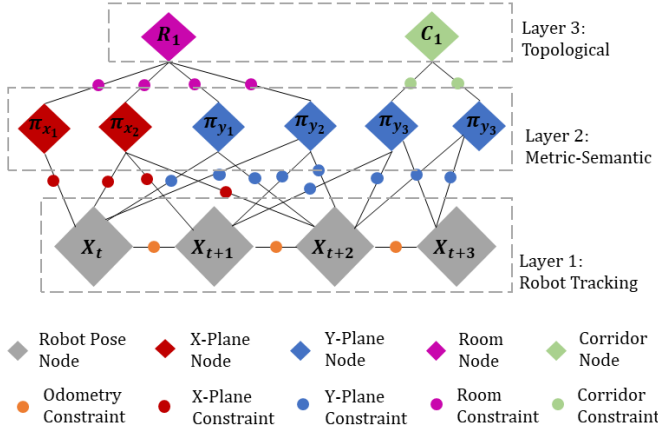


Fig. 3: Example of an S -Graph representing the robot pose, plane, room and corridor nodes together with their respective constraints.

robots, we also used in our S -Graphs the odometry from the encoders of these platforms.

D. Scene Mapping with S -Graphs

This module takes as inputs the robot odometry as well as the extracted planes to create the three-layered situational graph that simultaneously optimizes the robot states ${}^M\mathbf{x}_{R_t}$, $t \in \{1, \dots, T\}$ as well as the environmental model represented as a scene graph (see Fig. 3). We explain this module using the three layers of the graph.

Robot Tracking Layer. This layer creates a factor node ${}^M\mathbf{x}_{R_t} \in SE(3)$ with the robot pose at time t in the map frame M . The pose nodes are constrained by pairwise odometry readings between consecutive poses ${}^{R_{t-1}}\tilde{\mathbf{x}}_{R_t} \in SE(3)$. The associated cost function to minimize is

$$c_{\mathbf{x}}({}^M\mathbf{x}_{R_1}, \dots, {}^M\mathbf{x}_{R_T}) = \sum_{t=2}^T \|\boxplus {}^M\mathbf{x}_{R_{t-1}} \boxminus {}^M\mathbf{x}_{R_t} \boxminus {}^{R_{t-1}}\tilde{\mathbf{x}}_{R_t}\|_{\Lambda_{\tilde{\mathbf{x}}}}^2, \quad (4)$$

where we use \boxplus and \boxminus as the composition and inverse composition [29] and $\Lambda_{\tilde{\mathbf{x}}}$ is the information matrix associated to the odometry reading.

Metric-Semantic Layer. This layer creates the factor nodes for the planar surfaces extracted by the planar segmentation module. The planar normals extracted in the LiDAR frame L_t at time t are transformed to the global map frame M for its map representation

$$\begin{bmatrix} {}^M\mathbf{n} \\ {}^M d \end{bmatrix} = \begin{bmatrix} {}^M\mathbf{R}_{L_t} & 0 \\ -{}^M\mathbf{t}_{L_t} & 1 \end{bmatrix} \begin{bmatrix} {}^{L_t}\mathbf{n} \\ {}^{L_t}d \end{bmatrix} = {}^M\mathbf{T}_{\pi_t}({}^M\mathbf{x}_{R_t}) \begin{bmatrix} {}^{L_t}\mathbf{n} \\ {}^{L_t}d \end{bmatrix} \quad (5)$$

where we define ${}^M\mathbf{T}_{\pi_t}$ as the matrix that transforms the plane normal and distance from the LiDAR frame L_t to the map frame M . Such matrix is composed by the rotation matrix ${}^M\mathbf{R}_{L_t}$ and translation vector ${}^M\mathbf{t}_{L_t}$ between the LiDAR frame L_t and map frame M .

The plane normals with their ${}^M n_x$ or ${}^M n_y$ components greater than than the ${}^M n_z$ component are classified as

corresponding to vertical planes. Within the vertical planes, those with normals where ${}^M n_x$ is greater than ${}^M n_y$ are classified as x -plane normals, and otherwise they are classified as y -plane normals. Finally, planes whose normals' bigger component is ${}^M n_z$ are classified as horizontal planes.

Following [3], [30] we use the minimal plane parametrization ${}^M\boldsymbol{\pi} = [{}^M\phi, {}^M\theta, {}^M d]$, where ${}^M\phi$ and ${}^M\theta$ are the azimuth and elevation of the plane in the frame M . The cost to minimize for each plane observation ${}^{L_t}\tilde{\boldsymbol{\pi}}_i$ is as follows:

$$c_{\boldsymbol{\pi}}({}^M\mathbf{x}_{R_t}, {}^M\boldsymbol{\pi}_i) = \sum_{t=1, i=1}^{T, P} \|{}^{L_t}\boldsymbol{\pi}_i - {}^{L_t}\tilde{\boldsymbol{\pi}}_i\|_{\Lambda_{\boldsymbol{\pi}_{i,t}}}^2 \quad (6)$$

where the predicted plane normal ${}^{L_t}\mathbf{n}$ and distance ${}^{L_t}d$ in the LiDAR frame are computed from the plane estimates and robot pose as follows

$$[{}^{L_t}\mathbf{n} \quad {}^{L_t}d]^\top = {}^{L_t}\mathbf{T}_{\pi_t}({}^M\mathbf{x}_{R_t}) [{}^M\mathbf{n} \quad {}^M d]^\top \quad (7)$$

and the azimuth and elevation angles in the LiDAR frame, for Eq. 6, are extracted from the plane normal (${}^{L_t}\phi = \text{atan2}({}^{L_t}n_y, {}^{L_t}n_x)$) and ${}^{L_t}\theta = \text{atan2}({}^{L_t}n_z, \sqrt{{}^{L_t}n_x^2 + {}^{L_t}n_y^2})$.

After initializing each plane in the global map, correspondences are searched for every subsequent plane observations. We use the Mahalanobis distance between each mapped plane and the new extracted ones.

Topological Layer. The topological layer assesses if the mapped planes belong to a particular object or structural component and further constrain their geometry. In this work, we use room and corridor nodes, which can be both represented as a set of planes, although this could be easily extended to other structural topologies. We define a room node as composed of four planar walls, and similarly a corridor node as composed of two parallel wall planes.

For room nodes, if the metric-semantic layer at the robot node t identifies four planar surfaces (two x -planes π_1 and π_2 and two y -planes π_3 and π_4), the following tests are performed:

$${}^M\mathbf{n}_1 \cdot {}^M\mathbf{n}_2 < 0, \quad {}^M\mathbf{n}_3 \cdot {}^M\mathbf{n}_4 < 0 \\ w_x = {}^M d_2 - {}^M d_1 > \lambda, \quad w_y = {}^M d_4 - {}^M d_3 > \lambda \quad (8)$$

The dot product tests between the plane normals of the x -planes and the y -planes assess that the respective normals are opposed. w_x and w_y are the separation between the two x -planes and y -planes respectively, that should be greater than a threshold λ . In addition, the x - and y - plane pairs should be have similar extensions.

The room node ${}^M\boldsymbol{\rho} = [{}^M\rho_x, {}^M\rho_y, w_x, w_y]^\top$ is created using the planes satisfying the above criterion. The room center $[{}^M\rho_x, {}^M\rho_y]^\top$ is defined as

$$[\rho_x, \rho_y]^\top = [(\frac{w_x}{2} + {}^M d_1), (\frac{w_y}{2} + {}^M d_3)]^\top \quad (9)$$

Each room node is linked then to its corresponding x - and y - planes, and the total cost function to minimize is

$$c_{\boldsymbol{\rho}} = \sum_{j=1}^S \sum_{l=1}^4 c_{\rho_j, l}({}^M\boldsymbol{\rho}_j, \pi_l) \quad (10)$$

where for each room ${}^M\rho_j$, four costs, associated to each room-plane edge, are minimized (j index omitted for clarity and)

$$\begin{aligned} c_{\rho,1}({}^M\rho, \boldsymbol{\pi}_1) &= \left\| \left({}^M\rho_x - \frac{w_x}{2} \right) - {}^M\tilde{d}_1 \right\|_{\Lambda_\rho}^2 \\ c_{\rho,2}({}^M\rho, \boldsymbol{\pi}_2) &= \left\| \left({}^M\rho_x + \frac{w_x}{2} \right) - {}^M\tilde{d}_2 \right\|_{\Lambda_\rho}^2 \\ c_{\rho,3}({}^M\rho, \boldsymbol{\pi}_3) &= \left\| \left({}^M\rho_y - \frac{w_y}{2} \right) - {}^M\tilde{d}_3 \right\|_{\Lambda_\rho}^2 \\ c_{\rho,4}({}^M\rho, \boldsymbol{\pi}_4) &= \left\| \left({}^M\rho_y + \frac{w_y}{2} \right) - {}^M\tilde{d}_4 \right\|_{\Lambda_\rho}^2 \end{aligned} \quad (11)$$

Data association for the room node is also based on the Mahalanobis distance. We can safely tune the matching threshold close to the room widths, as rooms do not overlap. This allows us to merge planar structures duplicated due to inaccuracies.

Similarly to rooms, corridor nodes are created from either x -plane or y -plane pairs using the criteria in Eq. 8. For x -corridors ${}^M\boldsymbol{\kappa} = [\kappa_x, \kappa_y, w_x]$, and for y -corridors ${}^M\boldsymbol{\kappa} = [\kappa_x, \kappa_y, w_y]$. Analogously to the room factors in Eq. 9 and Eq. 11, we formulate the corridor nodes and edges linking them to their respective planes and minimize the summation of their associated costs $c_{\boldsymbol{\kappa}} = \sum_{k=1}^K c_{\boldsymbol{\kappa}_k}$. Assuming k corresponds to an x -corridor, for example, the cost to minimize would be $c_{\boldsymbol{\kappa}_k} = \sum_{l=1}^2 c_{\boldsymbol{\kappa}_k,l}({}^M\boldsymbol{\kappa}_k, \boldsymbol{\pi}_l)$, where $c_{\boldsymbol{\kappa},1}({}^M\boldsymbol{\kappa}, \boldsymbol{\pi}_1) = \left\| \left({}^M\kappa_x - \frac{w_x}{2} \right) - {}^M\tilde{d}_1 \right\|_{\Lambda_\kappa}^2$ and $c_{\boldsymbol{\kappa},2}({}^M\boldsymbol{\kappa}, \boldsymbol{\pi}_2) = \left\| \left({}^M\kappa_x + \frac{w_x}{2} \right) - {}^M\tilde{d}_2 \right\|_{\Lambda_\kappa}^2$. As before, Λ_κ stands for the information matrix of the observation

E. Loop Closure

In our pipeline, the loop closure is performed in a two-stage fashion. Firstly, each planar structure with its corresponding room and corridor node, adds a soft loop closure constraint optimizing the robot pose and the planar estimates mostly surrounding the room/corridor. While this soft loop constraint proves to be sufficient for environments with small areas or small robot odometry errors, an appearance-based loop closure constraint is essential in the opposite case of large odometric drifts. Hence, we also incorporate scan matching-based hard loop closure constraints modelled as edges at the robot tracking layer. The hard loop closure constraint is similar to the one implemented in [3], based on the Normal Distribution Transform-based scan matching. It uses a translational thresholding between the robot pose nodes to identify the loop closure candidates, and optimizes not only the robot poses but all the layers of the S -Graph.

IV. EXPERIMENTAL VALIDATION

We validate our S -Graphs on both simulated and real-world indoor scenarios, comparing it against several state-of-the-art LiDAR SLAM frameworks. We use the Gazebo¹ physics simulator to recreate indoor environments along with the simulated version of the Boston Dynamics Spot² robot mounted with a Velodyne VLP-16 3D LiDAR as our

¹<http://gazebosim.org/>

²<https://www.bostondynamics.com/products/spot>

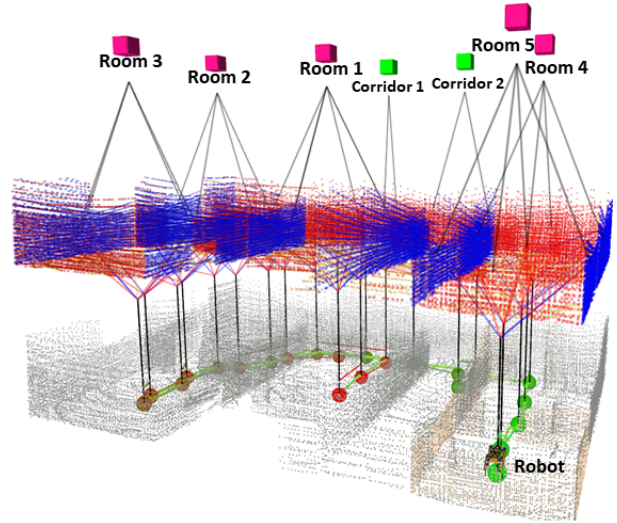


Fig. 4: S -Graph for the $SE-1$ experiment, demonstrating the creation of the three-layered situational graph. The robot nodes from the tracking layer are linked to the plane nodes from the metric-semantic layer, and plane nodes connected to the room/corridor nodes in the topological layer.

validation platform. In the real-world experiments, we use a Spot platform equipped with the VLP-16 LiDAR, navigating through office environments as well as real construction scenarios. Our code is built in C++ on top of the existing framework [3] and tested on-board an Intel i9 16 core workstation. A video of the experimental evaluation is available at <https://youtu.be/eoWrBTY040c>

A. Simulated Experiments

We conduct a total of four simulated experiments. Two of them were generated from the 3D mesh of two floors of actual architectural plans provided by a construction company, with different configurations of walls, rooms and corridors. We denote these two settings as Construction Floor-1 ($CF-1$) and Construction Floor-2 ($CF-2$). We also generated two additional simulated environments resembling typical indoor environments. The first one comprises six rooms and two narrow corridors and we denote it as Simulated Environment-1 ($SE-1$), and the second one comprises four bigger rooms and three corridors and we refer to it as Simulated Environment-2 ($SE-2$). In all the simulated experiments, the legged robot is commanded to navigate through the environments performing several rounds and finally returning to the initial position. Also in all the simulated experiment the robot encoders were not used for the odometry, which was estimated only from LiDAR. As some of the baselines cannot incorporate such robot odometric constraints, we ensure in this manner a fair comparison against the baselines.

We compared S -Graph against six state-of-the-art LiDAR SLAM approaches. Table. I shows the absolute trajectory error (ATE) [32]. We discarded LeGO-LOAM [21], as it did not provide reliable results on our experiments. This was due to its dependence of ground planes, which are not

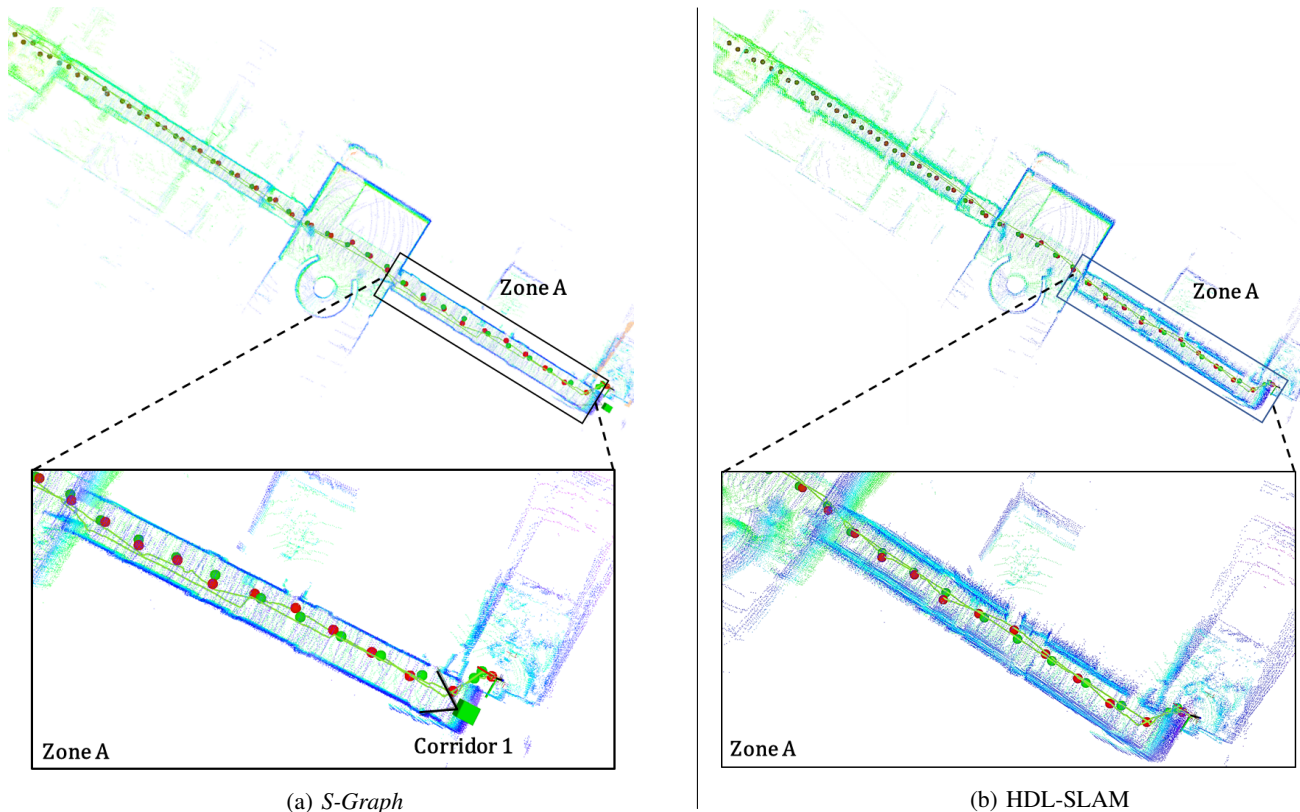


Fig. 5: Top view of the 3D maps estimated from the real data stream *LC-1* with our *S-Graph* (a) and with the baseline HDL-SLAM [3] (b). The zoomed-in views show the details of the mapped environment for Zone A. Note the “cleaner” reconstruction of the walls by our *S-Graph*, indicating a more accurate alignment than HDL-SLAM.

TABLE I: Absolute Trajectory Error (ATE) [m], of our *S-Graph* and several baselines on simulated data. Best results are boldfaced, second best are underlined.

Method	Dataset			
	<i>CF-1</i>	<i>CF-2</i>	<i>SE-1</i>	<i>SE-2</i>
HDL-SLAM [3]	0.09	<u>0.11</u>	<u>0.04</u>	<u>0.15</u>
ALOAM [1]	0.07	0.10	0.16	0.32
MLOAM [12]	0.15	0.39	0.65	2.82
FLOAM [11]	3.90	0.44	0.15	0.24
SCA-LOAM [31]	0.45	0.43	0.43	0.64
LIO-MAPPING [14]	0.35	0.35	0.29	0.45
<i>S-Graph - w/o top layer</i>	<u>0.05</u>	0.17	0.40	1.01
<i>S-Graph (ours)</i>	0.04	0.07	0.03	0.05

present all the time in our datasets. π -LSAM [23], does not have an open-source implementation and could not be included in the evaluation either. As observed in the table, our *S-Graph* incorporating the entire situational graph outperforms the baselines by a considerable margin, being the second best HDL-SLAM [3]. *S-Graph* also outperforms, by an even larger margin, other 3D LiDAR odometry and mapping systems, mainly the LOAM variant family. One of the reasons behind the higher errors of the LOAM-based variants is the use of feature-based odometries, as opposed to the VGICP-based odometry used by HDL-SLAM and our *S-Graph*, which demonstrates higher accuracy. Note, however, the additional improvement given by the addition of higher-

level graph levels comparing our *S-Graph* against HDL-SLAM. We ablated our model for further understanding of the importance of each layer, the row denoted *S-Graph - w/o top layer* corresponding to our model with only the two lower layers (robot tracking and metric-semantic). This result is further analyzed in Section. IV-C.

B. Real-World Experiments

We run five experiments on different structured indoor environments. All the methods utilize the odometry estimated by the robot encoders. The first two experiments are performed on two floors of an on-going construction site, the same scenes whose meshes were utilized to validate the algorithm in the simulated environment (*CF-1* and *CF-2*). The legged robot is navigated to traverse each floor several times, to assess the capability of the methods to maintain accurate estimates of the robot poses and the 3D map. To validate the accuracy of each method, we report the RMSE of the estimated 3D maps against the actual 3D map generated from the architectural plan (see Table. II). We also perform a similar experiment in an office environment with a long corridor (*LC-1*, see Fig. 5) that the robot traverses back and forth. Again, we compare the accuracy of the generated 3D map against the architectural plan of the office environment.

Finally, we perform experiments to assess the *S-Graph* performance with loop closure constraints in the large environments *LE-1* and *LE-2* (Fig. 6). *LE-1* comprises four

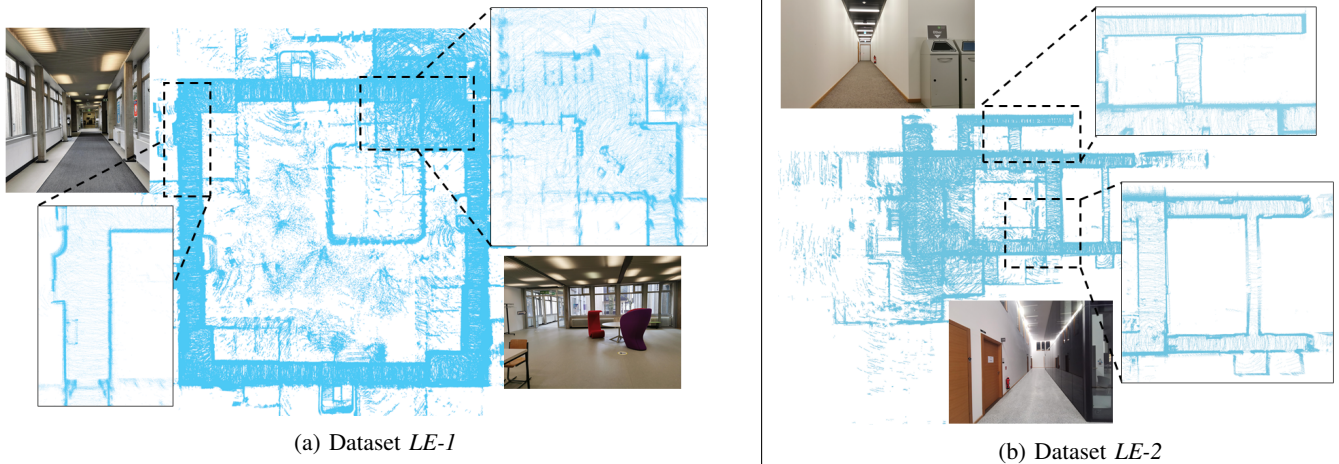


Fig. 6: Top view of the 3D maps estimated using *S-Graphs*. Zoomed-in views demonstrate the high quality of the wall reconstructions (constrained using corridor nodes). We also show pictures of the area for better understanding of the results.

TABLE II: Point cloud RMSE [m] on the real datasets. Best results are boldfaced, second best are underlined.

Method	Dataset		
	<i>CF-1</i>	<i>CF-2</i>	<i>LC-1</i>
HDL-SLAM	1.34	0.27	<u>1.45</u>
ALOAM	8.03	1.20	3.14
MLOAM	3.73	1.93	1.68
FLOAM	7.63	1.15	2.90
SCA-LOAM	4.86	0.75	2.89
<i>S-Graph - w/o top. layer</i>	<u>1.21</u>	0.24	<u>1.45</u>
<i>S-Graph (ours)</i>	0.94	<u>0.26</u>	1.32

corridors that the robot traverses three times. *LE-2* is a similar environment comprising additional corridors that the robot traverses twice. For both experiments, since the robot returns to the starting pose, we compute the pose error from the initial to the end point similarly to [23]. Table. III details the translational and rotational errors, demonstrating the accuracy of our approach in estimating the robot pose while generating accurate 3D map of the scene. A point to note in experiments *LE-1* and *LE-2* is that, although the robot was brought back to the initial point as carefully as possible, these metrics might be affected by errors of a few *mm*.

C. Ablation Study

To evaluate the accuracy of addition of our novel room/corridor factors to the situational graph, we repeat all the experiments disabling the corridor/room factors, only enabling the robot tracking layer and the metric-semantic layer. *S-Graph - w/o top. layer* in Table I presents the results in simulated datasets without the topological layer. It can be clearly seen the advantage of adding our novel room/corridor factors, in particular in the larger scenes of experiments *SE-1* and *SE-2*. In these two cases, the odometry drift causes erroneous plane matches, that are corrected due to the addition of the topological layer (explained in Sec. III-D). Similarly, *S-Graph - w/o top. layer* in Table II presents bigger errors in point cloud alignment in the absence of the topological layer. Observe also bigger error in larger

TABLE III: Translational [m] and rotational [$^{\circ}$] errors between the initial and end points for real datasets. Best results are boldfaced, second best are underlined.

Method	Metric	Dataset	
		<i>LE-1</i>	<i>LE-2</i>
HDL-SLAM	t_{err}	0.03	0.24
	r_{err}	0.17	0.06
ALOAM	t_{err}	1.78	<u>0.23</u>
	r_{err}	0.10	0.10
MLOAM	t_{err}	3.60	11.2
	r_{err}	0.04	0.42
FLOAM	t_{err}	7.22	9.28
	r_{err}	0.25	0.41
SCA-LOAM	t_{err}	0.55	0.93
	r_{err}	<u>0.08</u>	0.09
<i>S-Graph - w/o top. layer</i>	t_{err}	0.49	0.32
	r_{err}	0.12	<u>0.05</u>
<i>S-Graph (ours)</i>	t_{err}	<u>0.08</u>	0.11
	r_{err}	0.14	0.04

environments here and in Table III.

D. Limitations

Our *S-Graph* approach has shown promising results over all evaluated datasets, maintaining real-time performance for experiments with run times over 26 mins (Table IV). However, notice the larger computation times of the map optimizations compared to the baselines HDL-SLAM and ALOAM, which is expected due to the additional planar and room/corridor nodes and their constraints. We consider to address this limitation in future work by optimizing only the *S-Graph* nodes of the neighbouring region to the room/corridor that the robot is currently in.

V. CONCLUSION

In this paper we present *S-Graphs*, Situational Graphs for robots in structured environments, bridging the gap between low-level geometric SLAM and recent approaches targeting

TABLE IV: Average computation time [ms] of the most promising methods on real datasets.

Method	Dataset				
	CF-1	CF-2	LC-1	LE-1	LE-2
HDL-SLAM	4	3	8	20	10
ALOAM	3	2	4	5	5
<i>S-Graph (ours)</i>	70	83	83	250	330
Total runtime [s]	487	657	339	1321	1585

higher-level scene graphs. Our *S-Graphs* are composed of three layers. The *Robot Tracking Layer* optimizes a set of keyframe poses using odometric constraints. The *Metric-Semantic Layer* creates a dense metric-semantic map of the environment composed of planar surfaces, associating each plane with the keyframes in the robot tracking layer where they are visible. The *Topological Layer*, as the highest-level layer of the graph, connects the detected planar structures with our novel room/corridors factors.

We validated *S-Graphs* on simulated and real datasets captured by a legged robot in a construction site as well as in large structured indoor environments. We compared our approach against several relevant LiDAR-SLAM baselines, achieving state-of-the-art accuracy. This showcases that incorporating environment representations in the form of hierarchical *S-Graphs* do not only enhances the understanding of the environment, but also improves the state estimates. As a line for future work we plan to incorporate additional structural and dynamic constraints into *S-Graphs*, as well as to improve the room/corridor extraction and matching using works related to entire building model reconstruction [33].

REFERENCES

- [1] J. Zhang and S. Singh, "LOAM: Lidar Odometry and Mapping in Real-time," in *Robotics: Science and Systems*, 2014.
- [2] W. Hess, D. Kohler, H. Rapp, and D. Andor, "Real-time loop closure in 2D LIDAR SLAM," in *2016 IEEE International Conference on Robotics and Automation (ICRA)*, 2016, pp. 1271–1278.
- [3] K. Koide, J. Miura, and E. Menegatti, "A portable three-dimensional LIDAR-based system for long-term and wide-area people behavior measurement," *International Journal of Advanced Robotic Systems*, vol. 16, no. 2, Mar. 2019.
- [4] S. L. Bowman, N. Atanasov, K. Daniilidis, and G. J. Pappas, "Probabilistic data association for semantic SLAM," in *2017 IEEE International Conference on Robotics and Automation*, 2017, pp. 1722–1729.
- [5] H. Bavle, P. De La Puente, J. P. How, and P. Campoy, "VPS-SLAM: Visual Planar Semantic SLAM for Aerial Robotic Systems," *IEEE Access*, vol. 8, pp. 60704–60718, 2020.
- [6] X. Chen, A. Milioto, E. Palazzolo, P. Giguère, J. Behley, and C. Stachniss, "SuMa++: Efficient LiDAR-based Semantic SLAM," in *Proceedings of the IEEE/RSJ Int. Conf. on Intelligent Robots and Systems (IROS)*, 2019.
- [7] I. Armeni, Z.-Y. He, J. Gwak, A. R. Zamir, M. Fischer, J. Malik, and S. Savarese, "3D Scene Graph: A structure for unified semantics, 3D space, and camera," in *Proceedings of the IEEE/CVF International Conference on Computer Vision*, 2019, pp. 5664–5673.
- [8] A. Rosinol, A. Gupta, M. Abate, J. Shi, and L. Carlone, "3D dynamic scene graphs: Actionable spatial perception with places, objects, and humans," *arXiv preprint arXiv:2002.06289*, 2020.
- [9] C. Cadena, L. Carlone, H. Carrillo, Y. Latif, D. Scaramuzza, J. Neira, I. Reid, and J. J. Leonard, "Past, present, and future of simultaneous localization and mapping: Toward the robust-perception age," *IEEE Transactions on robotics*, vol. 32, no. 6, pp. 1309–1332, 2016.
- [10] R. Mur-Artal and J. D. Tardós, "ORB-SLAM2: an Open-Source SLAM System for Monocular, Stereo and RGB-D Cameras," *IEEE transactions on robotics*, vol. 33, no. 5, pp. 1255–1262, 2017.
- [11] H. Wang, C. Wang, C. Chen, and L. Xie, "F-LOAM : Fast LiDAR Odometry and Mapping," in *2021 IEEE/RSJ International Conference on Intelligent Robots and Systems (IROS)*, 2020.
- [12] J. Jiao, H. Ye, Y. Zhu, and M. Liu, "Robust Odometry and Mapping for Multi-LiDAR Systems With Online Extrinsic Calibration," *IEEE Transactions on Robotics*, pp. 1–10, 2021.
- [13] T. Shan, B. Englot, D. Meyers, W. Wang, C. Ratti, and D. Rus, "LIO-SAM: Tightly-coupled Lidar Inertial Odometry via Smoothing and Mapping," in *2020 IEEE/RSJ International Conference on Intelligent Robots and Systems (IROS)*. IEEE, 2020, pp. 5135–5142.
- [14] H. Ye, Y. Chen, and M. Liu, "Tightly Coupled 3D Lidar Inertial Odometry and Mapping," in *2019 IEEE International Conference on Robotics and Automation (ICRA)*. IEEE, 2019.
- [15] J. Graeter, A. Wilczynski, and M. Lauer, "LIMO: Lidar-Monocular Visual Odometry," in *2018 IEEE/RSJ international conference on intelligent robots and systems (IROS)*. IEEE, 2018, pp. 7872–7879.
- [16] T.-M. Nguyen, M. Cao, S. Yuan, Y. Lyu, T. H. Nguyen, and L. Xie, "LIRO: Tightly coupled lidar-inertia-ranging odometry," in *2021 IEEE International Conference on Robotics and Automation (ICRA)*. IEEE, 2021, pp. 14484–14490.
- [17] T. Shan, B. Englot, C. Ratti, and D. Rus, "LVI-SAM: Tightly-coupled Lidar-Visual-Inertial Odometry via Smoothing and Mapping," in *2021 IEEE International Conference on Robotics and Automation (ICRA)*. IEEE, 2021, pp. 5692–5698.
- [18] K. J. Doherty, D. P. Baxter, E. Schneeweiss, and J. J. Leonard, "Probabilistic data association via mixture models for robust semantic SLAM," in *2020 IEEE International Conference on Robotics and Automation (ICRA)*. IEEE, 2020, pp. 1098–1104.
- [19] A. Rosinol, M. Abate, Y. Chang, and L. Carlone, "Kimera: an open-source library for real-time metric-semantic localization and mapping," in *2020 IEEE International Conference on Robotics and Automation (ICRA)*. IEEE, 2020, pp. 1689–1696.
- [20] M. Grinvald, F. Furrer, T. Novkovic, J. J. Chung, C. Cadena, R. Siegwart, and J. Nieto, "Volumetric instance-aware semantic mapping and 3D object discovery," *IEEE Robotics and Automation Letters*, vol. 4, no. 3, pp. 3037–3044, 2019.
- [21] T. Shan and B. Englot, "LeGO-LOAM: Lightweight and Ground-Optimized Lidar Odometry and Mapping on Variable Terrain," in *2018 IEEE/RSJ International Conference on Intelligent Robots and Systems (IROS)*, 2018, pp. 4758–4765.
- [22] L. Li, X. Kong, X. Zhao, W. Li, F. Wen, H. Zhang, and Y. Liu, "SA-LOAM: Semantic-aided LiDAR SLAM with Loop Closure," in *2021 IEEE International Conference on Robotics and Automation (ICRA)*. IEEE, 2021, pp. 7627–7634.
- [23] L. Zhou, S. Wang, and M. Kaess, "π-LSAM: LiDAR Smoothing and Mapping With Planes," in *2021 IEEE International Conference on Robotics and Automation (ICRA)*, 2021, pp. 5751–5757.
- [24] L. Zhou, D. Koppel, and M. Kaess, "LiDAR SLAM With Plane Adjustment for Indoor Environment," *IEEE Robotics and Automation Letters*, vol. 6, no. 4, pp. 7073–7080, 2021.
- [25] A. Rosinol, A. Violette, M. Abate, N. Hughes, Y. Chang, J. Shi, A. Gupta, and L. Carlone, "Kimera: From SLAM to spatial perception with 3D dynamic scene graphs," *The International Journal of Robotics Research*, vol. 40, no. 12-14, pp. 1510–1546, 2021.
- [26] N. Hughes, Y. Chang, and L. Carlone, "Hydra: A Real-time Spatial Perception Engine for 3D Scene Graph Construction and Optimization," *arXiv preprint arXiv:2201.13360*, 2022.
- [27] P. Geneva, K. Eickenhoff, Y. Yang, and G. Huang, "LIPS: LiDAR-Inertial 3D Plane SLAM," in *2018 IEEE/RSJ International Conference on Intelligent Robots and Systems (IROS)*, 2018, pp. 123–130.
- [28] K. Koide, M. Yokozuka, S. Oishi, and A. Banno, "Voxelized GICP for Fast and Accurate 3D Point Cloud Registration," in *2021 IEEE International Conference on Robotics and Automation (ICRA)*, 2021, pp. 11054–11059.
- [29] J.-L. Blanco, "A tutorial on se(3) transformation parameterizations and on-manifold optimization," *University of Malaga, Tech. Rep.*, vol. 3, p. 6, 2010.
- [30] L. Ma, C. Kerl, J. Stückler, and D. Cremers, "CPA-SLAM: Consistent plane-model alignment for direct RGB-D SLAM," in *IEEE International Conference on Robotics and Automation*, 2016, pp. 1285–1291.
- [31] "Sc-a-loam," <https://github.com/gisbi-kim/SC-A-LOAM>, 2021.
- [32] M. Grupp, "evo: Python package for the evaluation of odometry and SLAM," <https://github.com/MichaelGrupp/evo>, 2017.
- [33] S. Ochmann, R. Vock, and R. Klein, "Automatic reconstruction of fully volumetric 3D building models from oriented point clouds," *ISPRS Journal of Photogrammetry and Remote Sensing*, vol. 151, pp. 251–262, 2019.